SUPPORTING INFORMATION

Structural characterization of the voltage sensor domain and voltage-gated K^+- channel proteins vectorially-oriented within a single bilayer membrane at the solid/vapor and solid/liquid interfaces via neutron interferometry

S. Gupta J. Dura, J.A. Freites, D.J Tobias and J. K. Blasie

MATERIALS

VSD & KvAP Proteins: The fully-hydrogenated isolated voltage sensor domain (VSD) protein from thermophilic archaebacteria *Aeropyrum pernix* (KvAP), in the absence of the PD but retaining a portion of the S4-S5 linker helix, was provided by Kenton Swartz's laboratory at NINDS, NIH. It was expressed in E. coli XL1-blue cells (Stratagene, Cat 200228) and purified by affinity chromatography, with the aid of a hexa-His-tag (His_6-tag) added to the C-terminus of the S4-S5 linker (C-terminal), and gel filtration.[1] MALDI-TOF mass spectrometry (Voyager-STR, PerSeptive Biosystems[11]) was utilized to verify the protein identity with an isotopically averaged molecular weight of 17276.38 g/mol (or ~17.276 kDa). A single mutant in the S3-S4 linker (A111→C111) was labeled with a polarity-sensitive, thiol-reactive fluorescent probe badan (6-bromoacetyl-2-dimethylamino-naphtalene).[2] VSD protein was solubilized at a concentration of 29 μM in pH 7.8 buffer containing 3% OG, 20 mM tris(hydroxymethyl)aminomethane (Tris) and 100 mM potassium chloride (KCl), to retain a mono-dispersed state. The full-length KvAP channel (average molecular weight of 100 kDa) solubilized in buffer at 6.4 μM containing 3.2% *n*-decyl-β-D-maltopyranoside (DM), 50 mM tris(hydroxymethyl)aminomethane (Tris) at pH 7.8 and 100 mM potassium chloride (KCl), was provided by Manuel Covarrubias' laboratory (Thomas Jefferson University, Jefferson Medical College, Philadelphia), following a protocol similar to that for VSD. Circular dichroism (CD) of detergent solubilized VSD and KvAP in buffer solution was carried out with Aviv CD spectrophotometer (Model 410, Lakewood, NJ) at 22 ^oC. The sample solutions were placed in a 1 mm quartz cuvette and the spectra were recorded over the UV range of 190-280 nm with a time constant of 20s, a spectral resolution of 1 nm and scan rate of 10 nm/min (see Fig. S2).

Chemicals: The nonionic detergent *n*-octyl-β-D-glucopyranoside (OG) and *n*-decyl-β-D-maltopyranoside (DM) were purchased from Anatrace (Maumee, OH) suitable for preserving the native conformation of membrane proteins. Neutral lipid 1-palmitoyl-2-oleoyl-*sn*-glycero-3-phosphocholine (16:0-18:1 PC; POPC) was purchased from Avanti Polar Lipids (Alabaster, AL) in chloroform solution. POPC was chosen to represent a prototypical membrane phospholipid for which the hydrocarbon core thickness of its bilayer form would approximately match the profile extent of the VSD's lateral hydrophobic surface. (3-Mercaptopropyl) trimethoxysilane (MPS) was obtained from Aldrich (St. Louis, MO), N-(5-(3-Maleimidopropionylamino)-1-carboxy-pentyl)iminodiacetic acid, disodium salt monohydrate (maleimido-C3-NTA) was from Dojindo Molecular Technologies (Rockville, MD). Bio-beads SM-2 Adsorbents was purchased from BioRad (Hercules, CA). All other reagents and solvents were obtained either from Fisher Scientific (Springfield, NJ) or Sigma-Aldrich (St. Louis, MO). All of the compounds were used

without further purification. The de-ionized (DI) water was supplied by a MilliQ system (18.4 MΩ-cm; Millipore Corp. Bedford, MA). Deuterated water (D_2O) (99.9% isotopic purity) was purchased from Cambridge Isotope Laboratories (Andover, MA).

Inorganic Multilayer Substrates: In order to increase the sensitivity and spatial resolution of neutron reflectivity enhanced by interferometry and possible magnetic phasing, multilayers comprised of 20 Å Si – 20 Å Ni – 50 Å Si and 30 Å Si – 30 Å Ni – 50 Å Si (referred to as Si-Ni-Si, here onwards) were deposited by DC magnetron sputtering onto 3" commercial Si(001) (p^+-Si:B – 525 μm thick) wafers purchased from El-Cat Inc. (Waldwick, NJ). This fabrication was performed in the Optics Fabrication and Metrology (OFM) laboratory in the X-ray Science Division at the Advanced Photon Source (APS), Argonne National Laboratory (ANL) (Argonne, IL).

METHODS: Protein immobilization and membrane reconstitution

Protein Immobilization: For SA approach, the Ni^{2+}-NTA terminated alkylated surface of the Si-Ni-Si substrate was incubated with VSD:OG or KvAP:DM solution that contained 2 μM protein in Tris buffer, pH 7.8 for more than 12 hours[3], and then rinsed several times with 1mM TRIS buffer and MilliQ water to remove nonspecifically bound protein. They were subsequently stored in a moist gas environment over a saturated salt solution in sealed vials providing > 90% relative humidity prior to the neutron reflectivity measurements.
Membrane Reconstitution: The surface tethered VSD:OG or KvAP:DM monolayer was incubated in 3 mL of 2 mg/mL POPC solution (pH 7.8, Tris buffer) with 0.9% OG or DM for approximately 1 hour, followed by adding ~ 400 mg of Bio-Beads to the solution as an OG/DM adsorbent, thus facilitating POPC exchange. At least 3-4 hours was employed to complete the exchange,[4,5] intended to reconstitute a POPC bilayer environment for the respective protein. They were subsequently rinsed with de-ionized (DI) water and stored in a humid gas environment glass in vials providing > 90% relative humidity prior to the neutron reflectivity measurements.

METHODS: Neutron interferometry at solid/vapor and solid/liquid interfaces:

Neutron Interferometry: Neutron interferometry (neutron reflectivity enhanced by interferometry) data were collected from self-assembled monolayers of VSD:OG, and reconstituted VSD:H-POPC and VSD:D4-POPC membranes at the solid/vapor and solid/liquid interfaces using methods described.[6,7] The versatility of the AND/R sample environment enabled stepwise characterization of the functionalized surface both for the monolayer and subsequently reconstituted bilayer membrane. Monochromatic cold neutrons of E = 3.3 meV (or $\lambda = 5$Å) were selected using a graphite monochromator with a wavelength spread of $\Delta\lambda/\lambda = 1\%$ that were reflected from the sample and counted with 2-inch pencil-type ^{3}He detector. Slit collimators reduced the incident beam divergence to ~0.016°. The detector acceptance angle was set at ~0.075° for reflectivity measurements (the specular component) and ~ 0.012° for the transverse scan (off-specular component). We collected neutron reflectivity data as a function of incident angle θ, using standard θ-2θ scans. Therefore, the reflected angle was maintained equal to incident angle translating to elastic momentum transfer, Q_z, analogous to X-ray reflectivity data. To account for background scattering, the off-specular component collected with the detector offset by ± 0.05° was subtracted from the specular data. In the off-specular experiment used to

establish the required offset, the detector was held fixed at an angle of $2\theta = 0.4^{o}$ with respect to the incident beam, while the sample was rocked from $0.1 < \theta < 0.3^{o}$. The θ-2θ scans employed accessed the Q_Z-range of $0.01 \leq Q_Z \leq 0.35$ Å^{-1} and required about 9 hours for each scan for each sample environment.

Solid/Vapor Interface: For the solid/vapor interface, the samples were transferred into a sealed cylindrical double-walled Al canister for providing environmental control without exposure to air and mounted *via* an Al clamp. The data were collected at solid/vapor interface where the relative humidity was controlled by a saturated salt solution of potassium nitrate (KNO_3) in water (100% H_2O) or deuterated water (100% D_2O) in high surface area glass containers within the canister yielding a moist gas environment of relative humidity (RH) ≅ 93%. The beam cross section of 1.5" x 1.5" was determined by the sample aperture and particular care was taken to minimize scattered neutrons entering the solid angle covered by the detector that were not scattered by the sample itself, achieved by shielding non-sample components in the canister with cadmium. The reflectivity data were collected in alternating fashion between 100% D_2O and 100% H_2O on the same specimen, allowing for equilibration of the exchange requiring less than one hour as monitored by the reflectivity at a particular Q_z (see Fig. S3).

Solid/Liquid Interface: For the solid/liquid interface, the specimens on 2x4 cm^2 slides were transferred into a specially designed wet cell intended for 3" diameter specimens. This cell is suitable for the AND/R instrument working in the backside reflection geometry *i.e.* the neutron beam is incident on the specimen through the thick underlying silicon instead of through humid gas as is the case for solid/vapor interface.[8] The smaller samples of 2x4 cm^2 were accommodated in the wet cell by placing a gasket made from a nitrile glove provide a seal between the sample surface and the front Al disk. The gasket was made according to the sample size exposing the sample area of ~ 1.84x3.84 cm^2. Prior to neutron reflectivity measurements an incident beam scan through thick fronting wafer is performed to measure incident beam intensity as a function of the indent angle. The subsequently measured neutron reflectivity from the specimens is normalized to this incident beam intensity. The specular reflectivity is measured between momentum transfers $0 \leq Q_z \leq 0.33$ Å^{-1}. The background scattering correction, utilizing an offset to either side of the specular ridge, was measured separately as described above. The background originated from incoherent scattering from bulk solvent, especially H_2O-based, and minimally from the nitrile gasket. In this way, two distinct data sets were collected for the same sample in contact with the isotopically different bulk solvents, namely bulk aqueous buffer with 100% D_2O or 60% D_2O/40% H_2O. All of the reflectivity data were reduced using the 'reflpak' software suite available from NCNR to provide the beam footprint and background corrected data.

For some of the solid/liquid interface measurements, the specimen on 1.7x1.7 cm^2 slides was transferred into a specially designed wet cell for 1" diameter Si suitable for the BL-4A (Magnetism Reflectometer; MR) instrument at the Spallation Neutron Source-ORNL working in the backside reflection geometry analogous to AND/R at the NIST-NCNR. The nitrile gasket was made such that it exposed a sample area of ~ 1.6x1.6 cm^2 to the incident neutron beam. All of the neutron reflectivity measurements for KvAP in 100% D_2O-based bulk aqueous buffer was performed at MR.[9] A wavelength band of 2.5-5.5 Å was chosen with a time-of-flight resolution of $\Delta\lambda/\lambda = 0.5\%$. Six incident beam angles ($\theta = 0.15^{o}$, 0.3^{o}, 0.6^{o}, 1.2^{o}, 2.4^{o} and 3.8^{o}) were used to cover a Q_z-range up to ~0.35 Å^{-1} for reflection from the solid/liquid interface with a constant angular resolution of 4.4%. A complete set of reflectivity data was obtained in about 5 h. All of these data were reduced with their custom software suite, namely 'REFreduction and REFscale' available from SNS-portal. After background correction, the raw data were normalized to

incident beam data recorded on the same day and divided by a constant factor to account for the incident beam slit size projected onto the sample (footprint correction).

For data collected on both the AND/R and BL-4A beamlines at the NIST-NCNR and ORNL-SNS, respectively, the incident beam dimensions were adjusted as a function of the angle of incidence in order to obtain a constant beam footprint on the specimen, which in turn gives rise to "footprint" correction due to the resulting change in incident neutron flux (see Fig. S4).

Due to the bulk aqueous environment, the value of the momentum transfer corresponding to the critical edge for total reflection, *i.e.* Q_c, key to the Fresnel-normalization, was expected to vary for different D_2O contents (60% and 100%) for the silicon/water interface (*i.e.*,0.0081 $Å^{-1}$ and 0.014 $Å^{-1}$, respectively), compared to that for the silicon/vapor interface (0.0103$Å^{-1}$). For all measured reflectivity data, while the multilayer reference structure remains relatively invariant upon exposure to organic and aqueous solvents, the critical-angle for total external reflection was found to vary by ~5-8% in Q_z compared to that calculated from the known composition and density of the substrate, progressing from the bare substrate to the tethered VSD:OG monolayer and on to the VSD:POPC membranes. This marginal variation in Q_c over the course of the interferometry experiments is likely due to Si and Ni interlayer diffusion (Figs. S5 and S6). We therefore allowed for this small variation in fitting the Fresnel function to the measured reflectivity data, a strategy similar to that used to determine electron density profiles from X-ray reflectivity data *via* constrained refinement. We thereby determined the neutron scattering-length density (nSLD or ρ_b) profiles for the tethered VSD:OG monolayer and the VSD:POPC membranes with $(Q_z)_{max} \cong 0.235$ $Å^{-1}$ both in 100% D_2O with a theoretical average ρ_b value of $+6.36 \times 10^{-6}/Å^2$, and in 60% D_2O/40% H_2O with a theoretical average ρ_b value of $+3.56 \times 10^{-6}/Å^2$.

Data Analysis Comment: Data reduction software available at the NCNR/NIST and the SNS/ORNL was used, as described above, to produce the background and footprint corrected specular neutron reflectivity data. Our method of analysis, involving a solution to the well known "phase problem", requires that these data be normalized by the Fresnel function representing the reflectivity from an ideally flat and smooth interface. The analytic form of this function was fit to each data set, employing a least-squares fitting routine as described previously, namely for the tethered VSD:OG (KvAP:DM) monolayer partially hydrated at the solid/vapor interface, the tethered VSD:OG (KvAP:DM) monolayer fully hydrated with bulk solvent at the solid/liquid interface, and all four cases prior to and following exchange against H-POPC/OG (H-POPC/DM) and D4-POPC/OG, along with the data for the Si-Ni-Si multilayer substrate itself in the same environments.

The Fresnel-normalized reflectivity data are then used to determine the average neuron scattering length density profile across the interface, i.e., along the z-direction perpendicular to the plane of the interface, employing a model-independent, constrained refinement algorithm implemented through Mathematica 4.2v (Wolfram Research, Champaign, IL)), that has been thoroughly described previously.[6] The "average" here arises from a projection of the structure parallel to the interface onto the normal to the plane of the interface. In the Distorted-Wave Born Approximation, the Fourier transform of the Fresnel-normalized data provides the autocorrelation function of the gradient electron density profile in the direction perpendicular to the interface for the Si-Ni-Si multilayer substrate itself, *versus* that for the substrate plus the bio-organic overlayer, both of which are bounded. This boundary constraint is one key input for the constrained refinement algorithm utilized to solve the classic "phase problem" in the derivation of the neutron scattering length density profiles. The corresponding autocorrelation functions

(also known as Patterson function) and absolute scattering length density profiles are shown in Figs. S5 and S6, for saturated water vapor (H_2O and D_2O, relative humidity of ~ 93%) and bulk solvent (100 %D_2O and 60%D_2O/40%H_2O) as representative examples, respectively. In the derivation of the latter profiles, the known scattering length density profile of the multilayer substrate itself, determined separately, is used as an additional key constraint in the refinement. We make the usual assumption that the structures of the bio-organic overlayers are invariant upon changing the D_2O/H_2O content of the environment, for either the moist or bulk aqueous cases, although D_2O and H_2O are known to have slightly different thermodynamic properties and hydrogen bonding characteristics due to differences in the OH and OD bonds' polarizability.[10] We also not that since our method of analysis require utilization of the Fresnel function, the H_2O content of the bulk aqueous environment was not reduced below 50%, since the observation of the critical-angle phenomenon in the reflectivity data is required for the Fresnel normalization. (see Fig. S7).

The neutron scattering length density (nSLD) of a material is a function of its atomic composition and density coupled with the corresponding nuclear scattering length (ρ_b) given by: $N_A \sum_i \frac{p_i}{A_i} b_i$, where N_A is Avogadro's number, p_i the mass density, A_i the atomic weight and b_i the nuclear scattering length of component i. These parameters for calculating various scattering length density profiles for a particular reference substrate with and without the presence of the tethered bio-organic overlayers also affect the critical angle [expressed as momentum transfer $Q_z = Q_c = 4\sqrt{\pi Nb}$)]for total neutron reflection from the interface, *albeit* marginally, but nevertheless necessary for the accurate calculation of the neutron scattering length density profiles and the subsequent *difference* profiles employed in this work.

Propagation of Errors: The errors (represented as the standard error) are shown explicitly in the background and footprint corrected reflectivity data shown in Figures 2, 5 and 11 (the error bars are more readily apparent on magnification and are seen to be equivalent to the point-to-point fluctuations throughout the Qz-range accessed in these experiments). The Fresnel normalization involves the fitting of the analytic Fresnel function to the reflectivity data in the vicinity of the critical-angle Q_c, which does not affect these errors since the error bars in this region are exceedingly small compared with those for $Q_z>Q_c$. The resulting Fresnel-normalized data for $Q_z>Q_c$ is subject to subsequent analysis. Our method of analysis employs Fourier transform and inverse Fourier transform operations, which obscures propagation of these errors that will be addressed below. However, we note here that convergence of the constrained refinement results in a *calculated* Fresnel-normalized reflectivity that lies well within these errors in the *experimental* Fresnel-normalized reflectivity data.

In order to address the propagation of errors in the reflectivity data into the derived neutron SLD profiles, we adopt the following procedure, with reference to Figure 8 (upper left-side). We utilize this figure as a representative example only because it shows the slab-model fit to the neutron SLD profiles for the *entire* structure, namely the multilayer Si-Ni-Si substrate with the bio-organic overlayer (VSD/OG in this case). Given the positions of the interfaces and the neutron SLD amplitudes of the steps in the refined 3-slab models for the VSD/OG monolayer, we systematically varied these positions and amplitudes one-at-a-time until the difference between the *calculated* Fresnel-normalized reflectivity and the *experimental* Fresnel-normalized reflectivity exceeded the errors in the latter data. In this manner, for the slabs defining the major features in the profiles, namely the two with neutron SLD's in excess of 0.5 x 10^{-6}/Å^2, the

positions of the interfaces are accurate to within ±3Å (~5% of the monolayer thickness) and the amplitude of the steps to within ±0.4 x 10^{-6}/Å^2. For the slab representing the minor feature on the proximal side (with respect to the substrate) of these profiles, the so-determined accuracy is necessarily less, namely ±10Å for the position of the interface nearest the substrate while the accuracy in its amplitude remains similar to that for the major features, namely ±0.3 x 10^{-6}/Å^2. Variation of these parameters two-at-a-time, addressing correlation, indicated that the effects of the uncertainties were generally larger by the same measure, than for variation of either parameter alone. The levels of uncertainty noted arise from the large neutron SLD contrast present in these Si-Ni-Si multilayer reference structures. Lowering the contrast in the reference structure using Si-Ge-Si, for example, would enhance sensitivity to the features of the bio-organic overlayer and reduce these uncertainties (and conversely). Lastly, we note that the same procedure has been applied to the slab-model profiles shown in Figures 7, 9 and 10 with entirely similar results for the so-determined uncertainties.

Exchangeable Hydrogen Comment: While the inorganic multilayer substrates and the phospholipid molecules utilized in this work contain no exchangeable hydrogen atoms, it is well known that there are exchangeable hydrogen atoms in proteins[11]. Furthermore, it can be expected that these exchangeable hydrogen atoms will indeed exchange, at least for those regions of the protein even transiently in contact with water, on the relatively long time-scales of the neutron reflectivity experiments. As a result, it is essential to take such exchange into consideration upon a change in D_2O/H_2O content of the protein's environment, irrespective of whether it is moist gas for the solid/vapor interface or bulk aqueous buffer for the solid/liquid interface (see Fig. S8).

METHODS: Molecular Dynamics Simulations:

Tethered VSD:POPC Membrane at the Solid/Liquid Interface: The atomistic model of the VSD consisted of residues 6 to 147 of KvAP channel. The S1-S4 segments and the S4-S5 linker correspond to residues 24 to 147 of the KvAP full channel model proposed by Lee et al. [12]. The remaining N-terminal segment (residues 6 to 23) was modeled as an amphiphatic helix using the so-called S0 helical domain of the Kv1.2 paddle-chimera structure [13] as a template. A thrombin cleavage sequence (LVPRGSRS) and a hexa-His-tag were added to the VSD C-terminal as an extended chain. The initial protein configuration was prepared by adding these extra N-terminal and C-terminal segments to the end configuration of a simulation trajectory of the KvAP VSD (residues 24 to 147) in a POPC bilayer with excess water [14]. The system so-constructed was submitted to 1152 steps of conjugate-gradient energy minimization and 100 ps at constant volumen and temperature (300 K) during which the backbone atoms of the original protein configuration (residues 24 to 147) were submitted to harmonic restraints. The final step of initial equilibration consisted of a 5 ns unrestrained run at constant temperature (300 K) and constant pressure (1 atm).

To model the fully hydrated supported bilayer system, the simulation cell was extended to 300 Å along the transmembrane direction to create an air/water interface on the distal side of the bilayer, and a12-3 integrated Lennard-Jones potential [15] was placed on the proximal side of the bilayer right under the bottommost layer of bulk water. The Lennard-Jones potential

coefficients were chosen to model the oxygen-oxygen interactions between SiO_x and water. Because 3-D periodic boundary conditions were used during the simulation, the repulsive component of the Lennard-Jones potential was also placed on the opposite end of the simulation cell to prevent evaporated waters from the distal side to reach the proximal side. Tethering between the solid substrate and the VSD was modeled as a single hydroxyl-terminated PEG-5 chain fixed on the substrate end by a position harmonic restraint and interacting with the last two His side chains of the VSD hexa-His-tag via distance restraints. The supported bilayer simulation system consisted of 1 VSD, 232 POPC molecules, 12109 waters, 1 PEG-5 and 4 counterions for a total of 69,968 atoms. The simulation was carried out at constant temperature of 300 K and constant volume of 90.14 x 87.38 x 300 $Å^3$ for 42 ns.

The all-atom molecular dynamics trajectory was generated with the NAMD 2.7b2 software package [16]. The CHARMM22, CHARMM36 and CHARMM35 force fields [17-19] were used for the protein, the lipids and the PEG-5 chain, respectively, and the TIP3P model was used for water [20]. The smooth particle mesh Ewald (PME) method [21,22] was used to calculate electrostatic interactions, and the short-range real-space interactions were cut off at 10 Å, using a switching function. A reversible multiple-time-step algorithm [23] was used to integrate the equations of motion with time steps of 4 fs for electrostatic forces, 2 fs for short-range non-bonded forces and 1 fs for bonded forces. All bond lengths involving hydrogen atoms were held fixed using the SHAKE [24] and SETTLE [25] algorithms. A Langevin dynamics scheme was used for thermostatting. Molecular graphics and simulation analyses were performed with the VMD 1.9 software package [26] over the last 15 ns of the simulation trajectory.

Determination of In-plane Occupancies from MD Simulations for the KvAP:POPC Membrane: The relative in-plane occupancies of POPC lipids and KvAP were determined over the last 100 ns of a 270 ns all-atom MD simulation trajectory of the KvAP open state in a POPC bilayer in excess water, reported by Schow et al.[28] The KvAP lipid solvation shell was assumed to comprise all the lipid molecules within a cylinder with axis along the center of the pore domain and radius defined by the in-plane distance from the pore domain center to the first coordination shell of lipids around the voltage-sensing domains. This criterion is consistent with the bilayer-like arrangement of lipid molecule fragments observed in the structure of the Kv1.2 paddle-chimera channel[29]. The total in-plane area of the solvation shell was calculated using the mean value of the solvation shell radius distribution over the simulation trajectory. The lipid:protein molar ratio per monolayer was determined from the distributions of the number of lipids within the solvation shell in each monolayer as the average of the means.

(a)

VSD; LRG LSDLG GRVRN IG DV MEHP LV ELGVSYAALL SVIVVVVEYT MQL [**S1**] **SGE** YLVR LYLVDLILVI ILWADYAYRA YK [**S2**] SGDP AGYV KKTLY [**S3a**] EIP AL VPAGLLALIE GHLAG [**S3b**] **LGL** FR LVRLLRFLRI LLIIS [**S4**] RG SKF LSAIADAADK [**S4-S5 linker**]
PD; IRFYHLFGAVMLTVLYGAFAIYIVE [**S5**] YPDPNSSIKS VFDALWWAVVTAT [**P**] TVGYGDVVPATP [**Filter**] IGKVIGIAVMLTGISALTLLIGTVSNMFQKILV GE [**S6**] LV PRGSRS (thrombin cleavage site) His_6-tag (HH HHHH)

(b)

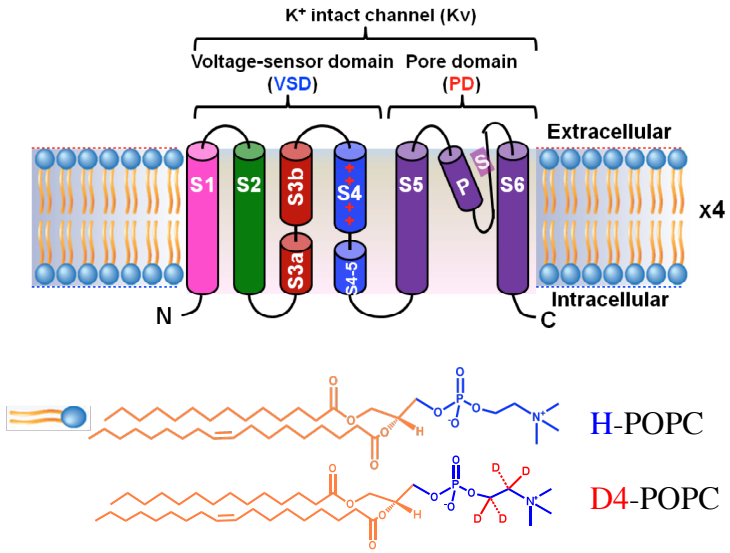

(c)

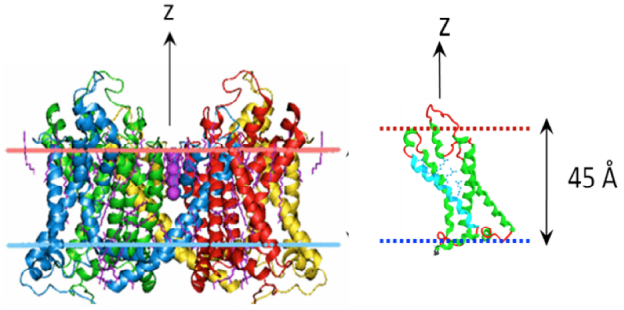

Figure S1. (Color online) (a) Amino acid sequence (one letter symbol) for VSD (L5-K147) and PD (I148-E242) from *Aeropyrum pernix* including hexa-His-tag. Schematic representations of spatial arrangement of the KvAP channel in a biophysical cell membrane. (b) A linear representation of one subunit from a full-length KvAP channel. The transmembrane-spanning segments, VSD (S1-S4) and PD (S5-S6) are color coded and α-helices are shown as cylinders connected through solid black loops. The positions of four positive Arginine residues in S4 segment responsible for voltage gating are marked with crosses. The tetrameric KvAP channel with one PD and four VSDs is also shown schematically. The relative positions of the four VSD's to PD are not definitive, likely depending on their different states (closed, activated, open, etc.), and display four-fold symmetry about the membrane normal in the open state. Shown is a single phospholipid molecule either fully-protonated (H-POPC) or specifically deuterated (D4-POPC) in the choline moiety with hydrophobic hydrocarbon chains (orange) and hydrophilic

polar headgroup (blue). (c) Ribbon representations of the transmembrane domain of full-length Kv1.2 (PDB *accession code* 2A79) X-ray crystal structure and isolated VSD within that structure bounded by lipid-like environment shown as horizontal dotted lines (shown here since the lipid-like environment utilized correctly positions the VSD relative to the PD).

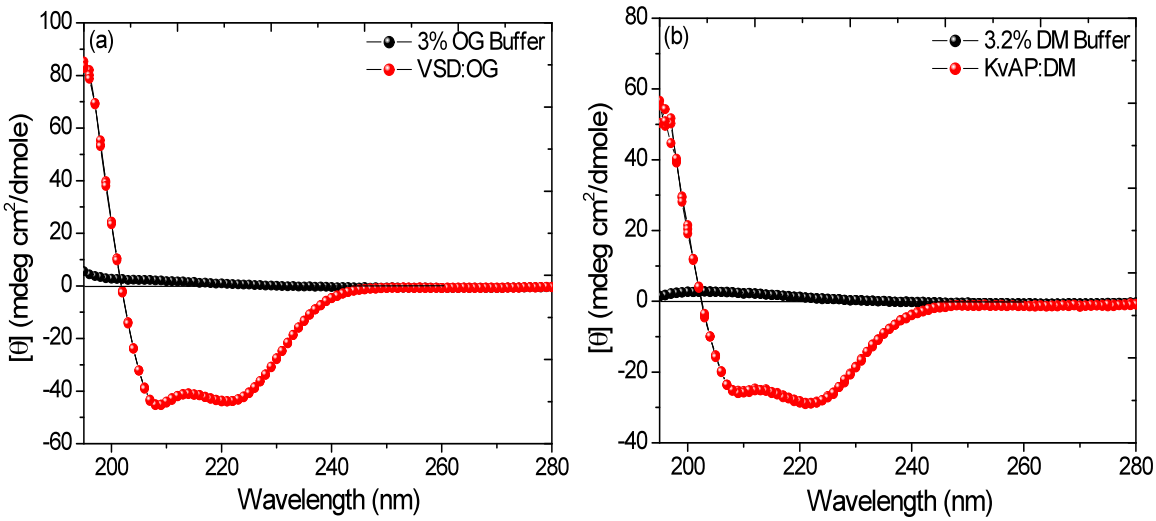

Figure S2. CD spectra of (a) VSD in (100 mM KCl, 20 mM Tris HCl, pH 7.8, 3% OG); (b) KvAP in (100 mM KCl, 20 mM Tris HCl, pH 7.8, 3.2% DM) detergent solution and the corresponding detergent-solution spectra as reference. The CD spectroscopy which is a qualitative tool to determine the chirality of organic molecules and the secondary structure [α-helix, β-sheet, β-turn and random coil] of biomolecules through differential absorption of left and right circularly polarized light *i.e.* $\Delta\varepsilon = \varepsilon_L - \varepsilon_R$ is proportional to [θ], reported as a degree of molar ellipticity. The spectra from both these solutions revealed a distinct minimum between 208 and 220 nm consistent with predominantly α-helical secondary structure within these proteins, the depth of the minimum indicative of a 70-80% helical content.

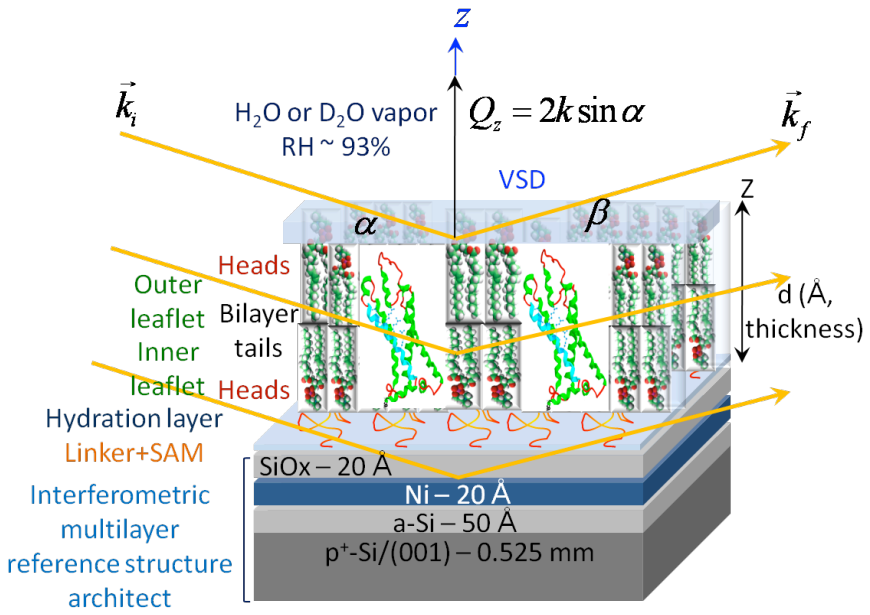

Figure S3. (Color online) A schematic representation of the interferometric approach to neutron reflectivity as a function of momentum transfer vector Q_z from vectorially-oriented VSD in a reconstituted POPC membrane at the solid/vapor interface (with Relative Humiditiy, RH ~ 93%) in front-side scattering geometry. The incident (k_i) and reflected (k_f) wavevector directions along with incident (α) and reflected (β) angles are shown (these angles are equal but not shown to scale for specular reflectivity). The different components of composite system are also labeled along Z direction.

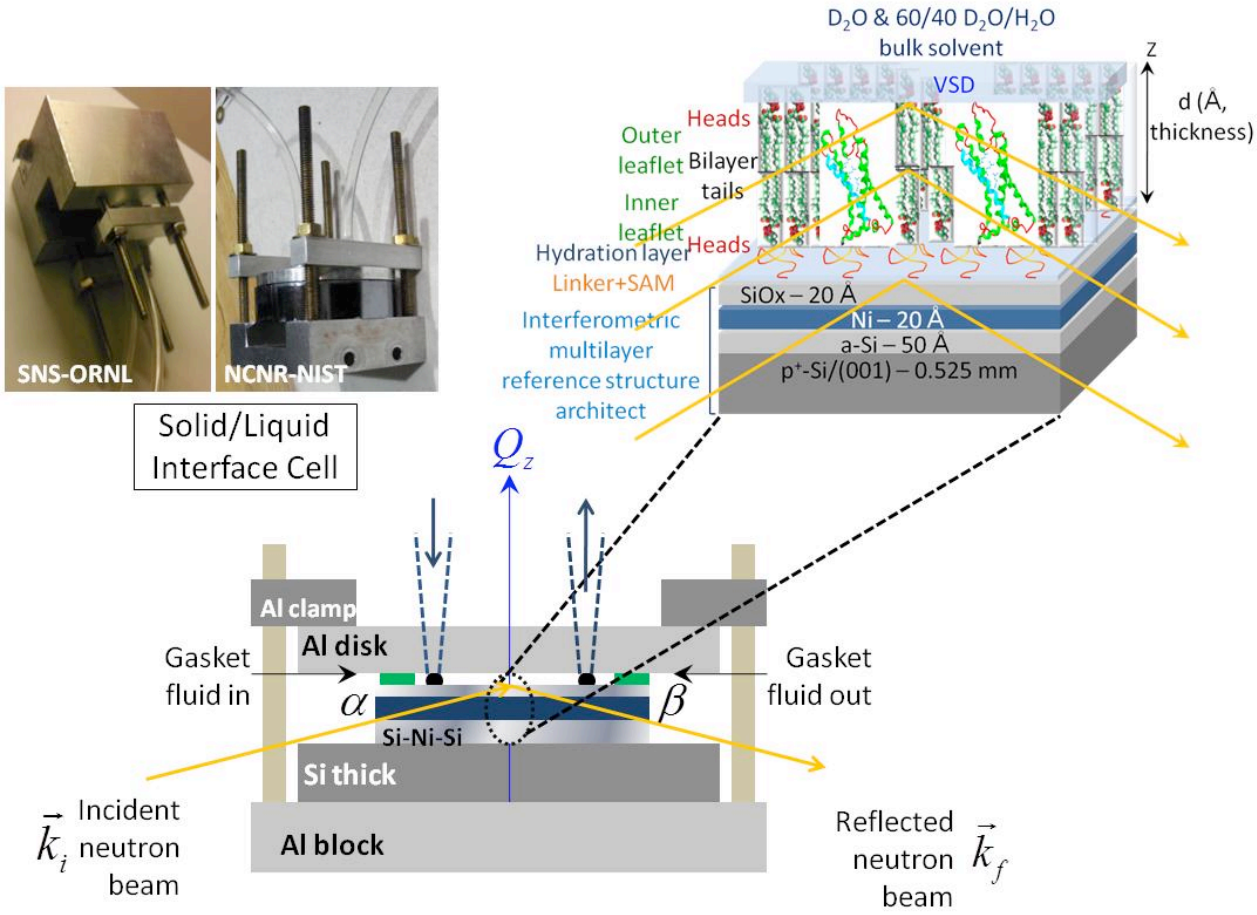

Figure S4. (Color online) Schematic side-view of the solid/liquid interface cell showing from bottom up, a back 3" diameter and 19 mm thick commercial Si wafer, 2x4 cm^2 Si-Ni-Si multilayer substrate possessing a bio-organic overlayer on its upper surface, front 3" diameter and 5 mm thick Al disk with two tapered holes attached to tubing that allows bulk solvent exchange via inlet and outlet, and 100 μm thick gasket on the front surface of specimen forming a reservoir, all mounted on a aluminum support held together with aluminum clamps and four brass alignment rods. Also shown are the photos of the wet cell for bulk solvent environment used at the NIST-NCNR (right) and the SNS-ORNL (left) facilities. The interferometric approach to neutron reflectivity as a function of momentum transfer vector Q_z from vectorially-oriented VSD in a reconstituted POPC membrane at the solid/liquid interface in back-side reflection geometry is expanded. The incident (k_i) and reflected (k_f) wavevector directions along with incident (α) and reflected (β) angles are also shown (these angles are equal, but not shown to scale for specular reflectivity).

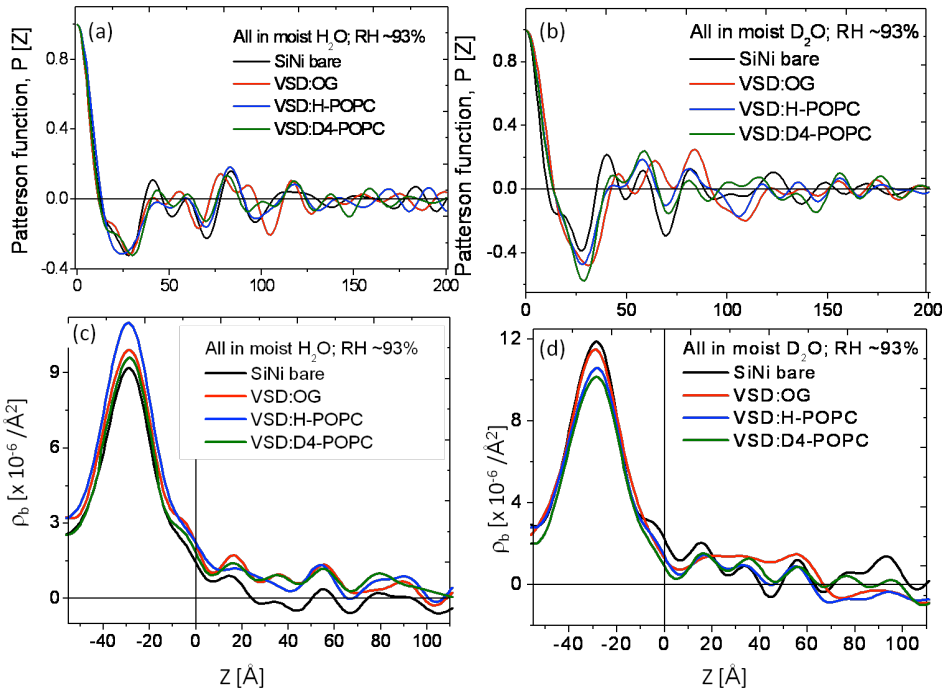

Figure S5. (Color online) Shown are the functions involved in the analyses of neutron interferometry data for the solid/vapor interface in terms of (a, b), the autocorrelation (or Patterson) function of the *gradient* of the neutron scattering length density profiles not requiring phase information and (c, d), the 'absolute' neutron scattering length density profiles derived from the phased data: (a, c) water (H_2O) and (b, d) deuterated water (D_2O) saturated vapor for the VSD:OG monolayer, VSD:H-POPC and VSD:D4-POPC membranes along with those for the multilayer reference structure itself in the same environment.

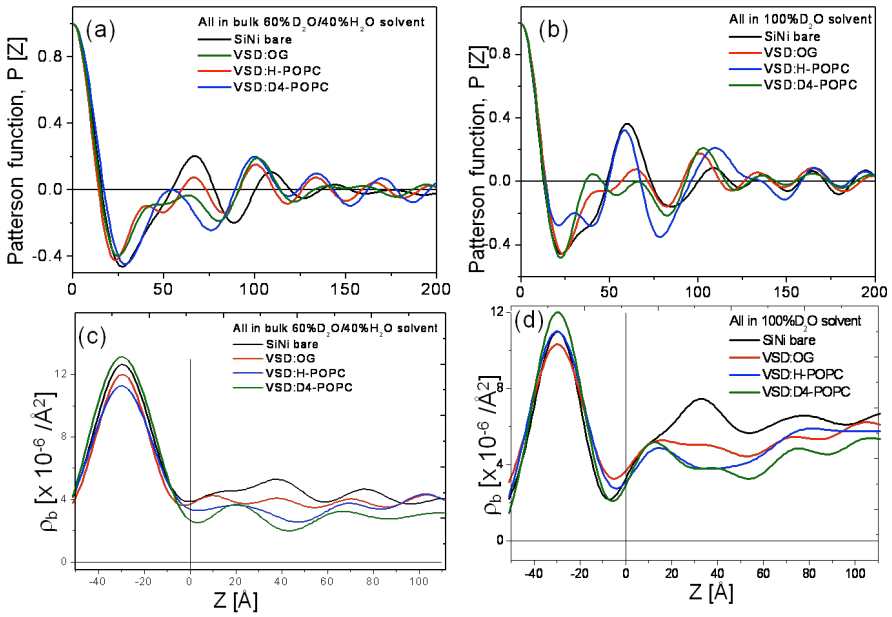

Figure S6. (Color online) Shown are the functions involved in the analyses of neutron interferometry data for the solid/liquid interface in terms of (a, b), the autocorrelation (or Patterson) function of the *gradient* of the neutron scattering length density profiles not requiring phase information and (c, d)), the 'absolute' neutron scattering length density profiles derived from the phased data: (a, c) 60%D_2O/40%H_2O and (b, d) 100% D_2O bulk aqueous solvent for the VSD:OG monolayer, VSD:H-POPC and VSD:D4-POPC membranes, along with those for the multilayer reference structure itself in the same environment.

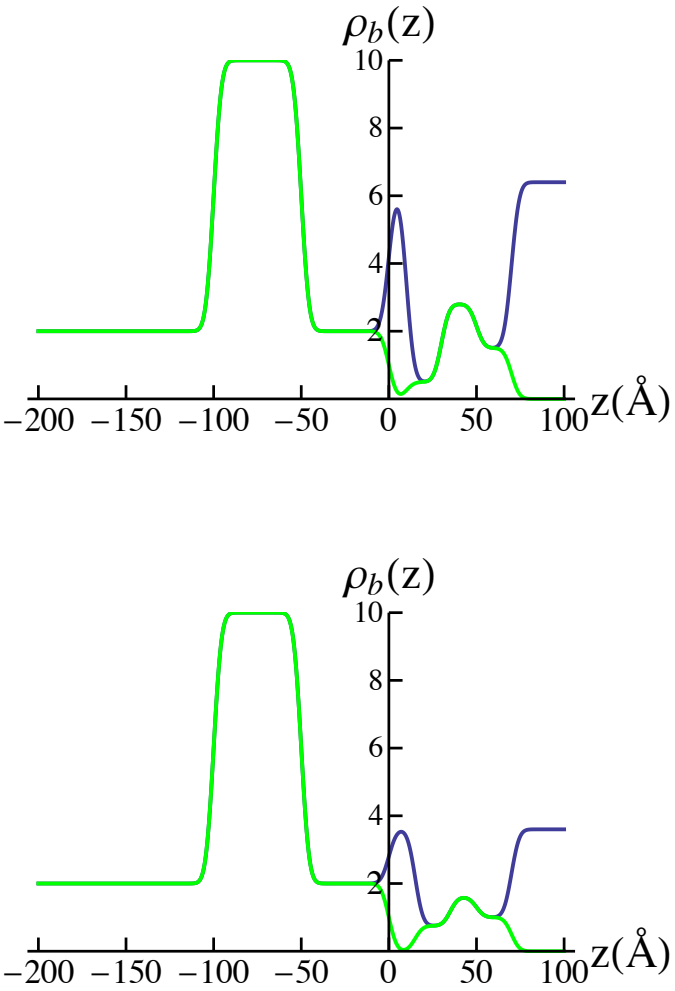

Figure S7. (Color online) Upper: VSD/OG slab-model profile moist-gas with D_2O (green) *versus as if* in bulk-water D_2O (blue), but assuming *no* structural changes, water penetration and/or H-D exchange within the VSD protein upon such an environmental change and that the VSD:OG complex occupies 100% of the monolayer in-plane area. Lower: VSD/OG in moist-gas with H_2O (green) *versus as if* in bulk-water 60% D_2O/40% H_2O (blue), again assuming *no* structural changes, water penetration and/or H-D exchange within the VSD protein upon such an environmental change *and* that the VSD:OG complex occupies 100% of the monolayer in-plane area. Si-Ni-Si multilayer substrate occurs for $z < 0$Å (green/blue superimposed). The differences in the slab-model profiles, here due to hydration with moist H_2O or D_2O, exceed the propagated error.

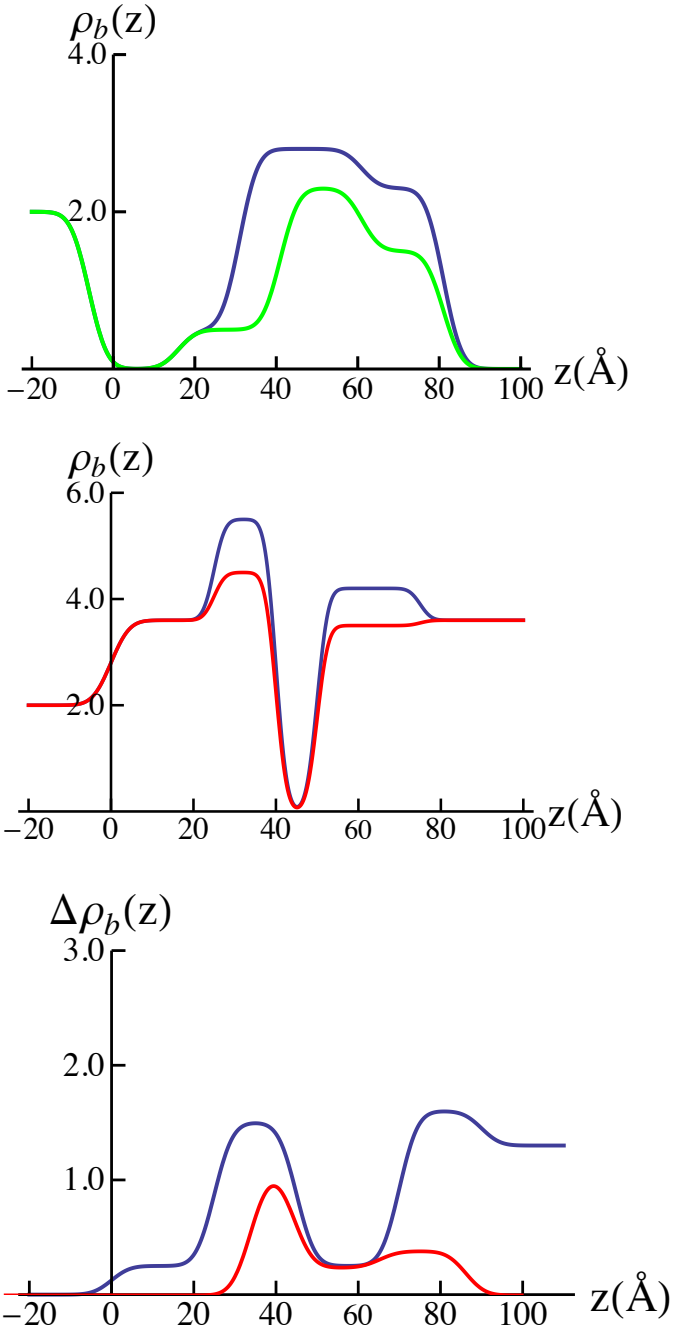

Figure S8: Summary of the slab-model profiles. Upper: refined 3-slab model for the VSD protein *within* the tethered VSD:OG monolayer, fully hydrated with 100% D_2O (blue) or 60%D_2O/40% H_2O (green), with the water slabs at either surface of the membrane removed as in moist-gas revealing the VSD itself. Middle: refined 3-slab models for the H-POPC (red) and D4-POPC (blue) bilayer within the reconstituted VSD:POPC membrane fully hydrated with 60%D_2O/40% H_2O. Lower: H-D exchange profile for the reconstituted VSD:POPC membrane (blue) and the H-D exchange profile for the VSD itself (red) within the membrane. The models for the VSD protein (upper) and H-D exchange profile for the VSD itself (lower, red) have been shifted slightly relative to the models for the POPC bilayer within the reconstituted VSD:POPC membrane (middle) by $\Delta z \sim 5$Å to allow for the slightly different positions of the VSD:OG monolayer and VSD:POPC membrane with respect to the substrate surface. The differences

in the slab-model profiles, here due to hydration with bulk H_2O or D_2O (top) and D4-POPC or H-POPC (middle), exceed the propagated error.

REFERENCES

(1) Krepkiy D.; Mihailescu M.; Freites J.A.; Schow E.V.; Worcester D.L.; Gawrisch K.; Tobias D.J.; White S.H.; Swartz K.J. *Nature* **2009**,*462*, 473-479.

(2) Koehorst R.B.M.; Spruijt R.B.; Vergeldt F.J.; Hemminga M. A. *Biophysical Journal* **2004**, *87*, 1445.

(3) Ataka, K., Giess F.; Knoll W.; Naumann R.; Haber-Pohlmeier S.; Richter B.; Heberle J. *Journal of the American Chemical Society* **2004**, *126*, 16199.

(4) Horigome T.; Sugano H. A rapid removal of detergents from protein solution. 1983. *Anal. Biochem.* **1983**, *130*, 393.

(5) Rohm and Haas, Surfactants-Handbook of Physical Properties, CS-16 G/cd, P7, Rohm and Haas, Philadelphia, PA.

(6) Kneller, L. R.; Edwards A.M.; Nordgren C.E.; Blasie J.K.; Berk N.F.; Krueger S.; Majkrzak C.F. *Biophysical Journal* **2001**, *80*, 2248 and references therein.

(7) McGillivray, D. J.; Valincius G.; Heinrich F.; Robertson J.W.F.; Vanderah D.J.; Febo-Ayala W.; …; Kasianowicz J.J. *Biophysical Journal* **2009**, *96*, 1547.

(8) Dura J. A., Pierce D.J.; Majkrzak C.F.; Maliszewskyj N.C.; McGillivray D.J.; Losche M.; V.o'Donovan K.; Mihailescu M.; P-Salas U.; Worcester D.L.; White S.H. *Rev. Sci. Instrum.* **2006**, *77*, 074301.

(9) Lauter V., H. Ambaye, R. Goyette, W.-T. Hal Lee, A. Parizzi, *Physica B- Condensed* Matter **2009**, *404*, 2543-2546.

(10) Marcus Y.; Ben-Naim A. *J. Chem. Phys*. **1985**, *83*, 4744-4759.

(11) Disclaimer: Certain commercial equipment, instruments, or materials (or suppliers, or software, ...) are identified in this paper to foster understanding. Such identification does not imply recommendation or endorsement by the National Institute of Standards and Technology, nor does it imply that the materials or equipment identified are necessarily the best available for the purpose.

(12) Lee, S.-Y.; Lee, A.; Chen, J.; MacKinnon, R. *Proc.Nat.Acad.Sci.USA* **2005**, *102*, 15441-15446.

(13) Long, S. B.; Tao, X.; Campbell, E. B.; Mackinnon, R. *Nature* **2007**, *450*, 376-382.

(14) Freites, J. A.; Tobias, D. J.; White, S. H. *Biophysical Journal* **2006**, *91*, L90-L92.

(15) Hautman, J.; Klein, M. L. *The Journal of Chemical Physics* **1989**, *91*, 4994.

(16) Phillips, J. C.; Braun, B.; Wang, W.; Gumbart, J.; Tajkhorshid, E.; Villa, E.; Chipot, C.; Skeel, R. D.; Kalé, L.; Schulten, K. *Journal of Computational Chemistry* **2005**, *26*, 1781-1802.

(17) MacKerell, A. D., Jr.; Bashford, D.; Bellott, M.; Dunbrack, R. L., Jr.; Evanseck, J. D.; Field, M. J.; Fischer, S.; Gao, J.; Guo, H.; Ha, S.; Joseph-McCarthy, D.; Kuchnir, L.; Kuczera, K.; Lau, F. T. K.; Mattos, C.; Michnick, S.; Ngo, T.; Nguyen, D. T.; Prodhom, B.; Reiher, W. E., III; Roux, B.; Schlenkrich, M.; Smith, J. C.; Stote, R.; Straub, J.; Watanabe, M.; Wiórkiewicz-Kuczera, J.; Yin, D.; Karplus, M. *J.Phys.Chem.B* **1998**, *102*, 3586-3616.

(18) Klauda, J. B.; Venable, R. M.; Freites, J. A.; O'Connor, J. W.; Tobias, D. J.; Mondragon-Ramirez, C.; Vorobyov, I.; MacKerell, A. D., Jr.; Pastor, R. W. *Journal of Physical Chemistry B* **2010**, *114*, 7830-7843.

(19) Vorobyov, I.; Anisimov, V. M.; Greene, S.; Venable, R. M.; Moser, A.; Pastor, R. W.; MacKerell Jr, A. D. *Journal of chemical theory and computation* **2007**, *3*, 1120-1133.

(20) Jorgensen, W. L.; Chandrasekhar, J.; Madura, J. D.; Impey, R. W.; Klein, M. L. *J.Chem.Phys.* **1983**, *79*, 926-935.

(21) Darden, T.; York, D.; Pedersen, L. *J.Chem.Phys.* **1993**, *98*, 10089-10092.

(22) Essmann, U.; Perera, L.; Berkowitz, M. L.; Darden, T.; Lee, H.; Pedersen, L. G. *J.Chem.Phys.* **1995**, *103*, 8577-8593.

(23) Grubmüller, H.; Heller, H.; Windemuth, A.; Schulten, K. *Molecular Simulation* **1991**, *6*, 121-142.

(24) Ryckaert, J.-P.; Ciccotti, G.; Berendsen, H. J. C. *Journal of Computational Physics* **1977**, *23*, 327-341.

(25) Miyamoto, S.; Kollman, P. *Journal of Computational Chemistry* **1992**, *13*, 952-962.

(26) Humphrey, W.; Dalke, W.; Schulten, K. *J.Mol.Graphics* **1996**, *14*, 33-38.

(27) Schow E.V.; Freites J.A.; Nizkorodov, A.; White S.H.; Tobias D.J. *Biochim. Biophys. Acta* **2012**, *1818*, 1726-1736.

(28) Long, S. B.; Tao, X.; Campbell, E. B.; Mackinnon, R. *Nature* **2007,** *450***,** 376-382.